Characterization and RSM-Based Modeling of Sustainable *Malva sylvestris* L./Polypropylene Composites

Mücahit Osman Türkan [a], Mustafa Öncül [b,*] and Melih Savran [b]

Malva sylvestris L. was evaluated as a potential sustainable lignocellulosic filler for polypropylene-based composites. Composites containing two particle size fractions and filler loadings ranging from 5 wt% to 20 wt% were produced through thermokinetic mixing and compression molding. Chemical, morphological, thermal, and mechanical characterizations were performed to determine the influence of filler incorporation on composite performance. The results showed that increasing filler content reduced tensile and flexural strengths by up to 27.2% and 29.6%, respectively, due to limited interfacial compatibility between the hydrophilic filler and hydrophobic polymer matrix. In contrast, the tensile and flexural moduli increased by up to 15.6% and 18.0%, respectively, indicating enhanced stiffness through restricted polymer chain mobility. Thermal analysis revealed improved thermal stability, with the onset degradation temperature increasing by approximately 35 °C at the highest filler loading. The filler particles also acted as heterogeneous nucleating sites, promoting earlier crystallization without substantially altering the degree of crystallinity. Mechanical properties were successfully modeled using response surface methodology. Linear model provided the most accurate predictions for tensile strength, whereas quadratic models better represented tensile modulus and flexural behavior. These findings demonstrate that *Malva sylvestris* L. is a promising renewable filler for lightweight polymer composites.

DOI: 10.15376/biores.21.3.7848-7870

Keywords: Polypropylene composites; Lignocellulosic filler; Response surface methodology; Mathematical modeling

Contact information: a: The Graduate School of Natural and Applied Sciences, Department of Mechanical Engineering, Izmir Katip Celebi University, Izmir, Türkiye; b: Faculty of Engineering and Architecture Department of Mechanical Engineering, Izmir Katip Celebi University, Izmir, Türkiye;
** Corresponding author: mustafa.oncul@ikcu.edu.tr*

INTRODUCTION

The increasing demand for sustainable materials has accelerated research on renewable and environmentally responsible alternatives to conventional petroleum-based products. Among these alternatives, lignocellulosic fiber-reinforced polymer composites have attracted considerable attention because of their low density, renewability, biodegradability, widespread availability, and favorable cost-performance balance. The utilization of agricultural residues and naturally occurring biomass resources in polymer composites also supports the principles of circular economy, industrial ecology, and sustainable manufacturing by reducing dependence on non-renewable resources and minimizing environmental impacts (Bharath and Basavarajappa 2016; Diambu and Çevik

2025). Consequently, natural fiber-reinforced composites have found increasing applications in automotive, construction, packaging, and consumer product sectors (Öncül *et al.* 2025).

Among thermoplastic polymers, polypropylene (PP) is one of the most widely used matrix materials because of its low density, low cost, excellent processability, chemical resistance, and industrial availability (Hossain *et al.* 2024). Numerous studies have demonstrated that the incorporation of lignocellulosic fillers into PP can improve stiffness while reducing material cost and environmental footprint (Abraha *et al.* 2023; Bahlouli *et al.* 2023; Öncül 2026). However, a major challenge in PP-based composites is the inherent incompatibility between the hydrophobic PP matrix and hydrophilic natural fibers. This polarity mismatch often results in poor interfacial adhesion, limited stress transfer, and reduced mechanical strength (Pokharel *et al.* 2022).

To overcome this limitation, compatibilizing agents such as maleic anhydride-grafted polypropylene (MAPP) are frequently incorporated into composite formulations. Incorporation of MAPP or related compatibilizing agents can enhance interfacial adhesion through improved physicochemical interactions between the hydrophobic matrix and hydrophilic reinforcement. Numerous studies have demonstrated significant improvements in mechanical performance following compatibilizer addition. However, before introducing interfacial modifiers, it is essential to evaluate the intrinsic compatibility and reinforcement potential of a novel lignocellulosic filler within the polymer matrix. Such baseline investigations provide fundamental insight into the natural filler–matrix interactions and enable the independent assessment of the effects of particle size, filler loading, and filler morphology. Therefore, compatibilizing agents were intentionally excluded from the present study to establish the inherent structure–property relationships of *Malva sylvestris* L. (MS)/PP composites and to provide a reference framework for future interface-engineering studies.

MS is a rapidly growing herbaceous plant widely distributed across Europe, Asia, North Africa, and the Mediterranean region. Its stems consist mainly of cellulose, hemicellulose, and lignin, with smaller amounts of pectin, waxes, and extractives. The relatively high cellulose content (approximately 40 to 50%) provides reinforcement potential, while the abundance of hydroxyl groups imparts a hydrophilic character that may limit compatibility with hydrophobic polymers such as PP (Nascimento *et al.* 2017). In addition, lignin contributes to structural rigidity and thermal stability, whereas pectins, waxes, and extractives can influence interfacial interactions. Although MS fibers have been investigated for textile, biomedical, and ballistic applications (Nascimento *et al.* 2017), the use of mechanically processed MS particles as fillers in PP composites remains largely unexplored. Furthermore, information regarding the structure–property relationships, thermal behavior, interfacial characteristics, and mechanical performance of PP composites reinforced with MS particles remains largely unavailable in the literature. This represents a significant research gap that warrants systematic investigation.

In addition to experimental characterization, predictive modeling approaches are increasingly employed to establish quantitative relationships between composite design variables and material performance. Response Surface Methodology (RSM) provides an effective statistical framework for evaluating the influence of multiple processing and material parameters while reducing experimental complexity (Savran *et al.* 2023). The method also facilitates optimization and supports the development of predictive equations for engineering applications.

Therefore, the objective of this study was to develop and characterize PP composites reinforced with MS particles for the first time. Two particle size fractions and filler loadings ranging from 5 wt% to 20 wt% were investigated. The chemical composition, morphology, thermal behavior, and mechanical performance of the resulting composites were systematically evaluated. Furthermore, RSM was employed to model the tensile and flexural properties using three regression selection techniques, namely Stepwise Regression, Forward Selection Regression, and Backward Elimination Regression. The findings provide new insight into the suitability of MS as a sustainable lignocellulosic filler and establish predictive relationships for future composite design and optimization.

EXPERIMENTAL

Materials

Commercial PP (LG M1500, South Korea) with a melt flow index of 16 g/10 min (230 °C, 2.16 kg) and a density of 0.9 g/cm³ was utilized as the polymer matrix. MS plants, used as the sustainable lignocellulosic filler, were harvested from the campus area of Izmir Katip Celebi University (İzmir, Türkiye), where the species grows naturally under low-input conditions.

Filler Preparation and Composite Production

PP was utilized as the polymer matrix, and MS was employed as the lignocellulosic filler. The stem sections of the harvested MS plants were separated, cleaned to remove surface impurities, and mechanically ground. The ground material was subsequently sieved to isolate two distinct particle size fractions: particles under 100 μm (MS1) and particles between 100 μm and 250 μm (MS2). Prior to compounding, the MS particles were dried in a ventilated oven at 60 °C for 24 h to minimize moisture content. Composite samples were formulated by incorporating these prepared fillers into the PP matrix at various weight fractions. Specifically, composites reinforced with MS1 were denoted as 5MS1, 10MS1, 15MS1, and 20MS1, corresponding to filler loadings of 5 wt%, 10 wt%, 15 wt%, and 20 wt%, respectively. Similarly, formulations incorporating MS2 particles at identical weight percentages were designated as 5MS2, 10MS2, 15MS2, and 20MS2. The composites were compounded using a high-speed thermokinetic mixer operated at a rotational speed of 2000 rpm. This generated frictional heating that raised the material temperature to approximately 190 °C, facilitating the melting of the polymer matrix and the uniform dispersion of the filler particles. The homogenized melt was subsequently transferred to a temperature- and time-controlled hot-cold hydraulic press (Gülnar Machine, Türkiye) and compression-molded into standardized samples for characterization. Detailed information regarding the thermokinetic mixing and compression molding procedures can be found in previous studies (Öncül 2023, 2026).

Characterization Methods

The chemical constituents of the MS filler were determined following TAPPI standard methods. The compositional analysis quantified the extractives TAPPI T 204 cm-97 (2007), lignin content TAPPI T222 om-02 (2006), holocellulose, and α-cellulose TAPPI T203 cm-99 (1999). The ash content was evaluated according to TAPPI T211 om-02 (2002).

Fourier transform infrared (FTIR) measurements were conducted using a Nicolet iS50 spectrophotometer (Thermo Scientific, Waltham, MA, USA). Finely ground samples were homogeneously mixed with infrared-grade potassium bromide (KBr) and compressed into transparent pellets. The spectra were recorded between 400 to 4000 cm^{-1} at a resolution of 2 cm^{-1} using 25 scans per sample.

Thermogravimetric analysis (TGA) was performed on an SDT Q600 STA analyzer (TA Instruments, New Castle, DE, USA). The samples were heated from 30 °C to 600 °C at a constant heating rate of 10 °C/min under a nitrogen atmosphere. Differential scanning calorimetry (DSC) was conducted using a Q2000 DSC (TA Instruments, New Castle, DE, USA) under a nitrogen atmosphere. To eliminate the thermal history, the samples were heated from 20 °C to 200 °C at 10 °C/min and held for 3 min, subsequently cooled to 20 °C at 10 °C/min, and reheated to 200 °C at the same heating rate.

The fracture surface morphologies were examined using a 300VP scanning electron microscope (SEM) (Carl Zeiss, Oberkochen, Germany) operating at an accelerating voltage of 5 kV. All samples were sputter-coated with a thin gold layer using a Q150 RES sputter coater (Quorum, East Sussex, UK) prior to observation to mitigate surface charging.

Tensile and three-point bending tests were performed using an AGS-X universal testing machine (Shimadzu Corporation, Kyoto, Japan) equipped with a 5 kN load cell. The tensile tests complied with the ASTM D638-22 (2022) standard utilizing a crosshead speed of 50 mm/min. The flexural tests complied with the ASTM D790-17 (2017) standard, utilizing a crosshead speed of 2 mm/min and a support span of 32 mm. A minimum of five replicate samples were tested for each formulation, and the average values with standard deviations were recorded to ensure statistical reliability.

Mathematical Modeling and Statistical Analysis

For statistical and mathematical modeling frameworks, RSM was employed, which created predictive relationships between the design parameters and the mechanical responses. The general second-order polynomial model was used as functional form in RSM as shown in Eq. 1,

$$Y = \beta_0 + \sum_{i=1}^{k} \beta_i x_i + \sum_{i=1}^{k} \beta_{ii} x_i^2 + \sum_{i=1}^{k} \sum_{i=j+1}^{k} \beta_{ij}\, x_i x_j + \varepsilon \quad (1)$$

where Y denotes the predicted response variable, x_i and x_j represent the independent design variables. The term β_0 corresponds to the intercept, β_i signifies the linear coefficients, β_{ii} represent the quadratic coefficients, β_{ij} denotes the interaction coefficients between the variables, and ε accounts for the random experimental error.

Three different RSM-based regression selection techniques, SR, FSR, and BER were systematically applied to determine the most appropriate model structure and identify statistically significant terms (Savran and Aydin 2024; Savran 2026). All modeling approaches initially considered the full quadratic polynomial model as the candidate architecture. The statistical adequacy and significance of the developed regression models were evaluated using Analysis of Variance (ANOVA). Furthermore, several statistical performance indicators, summarized in Table 1, were employed to assess the predictive capability of the models (Savran and Aydin 2024; Özçiçek *et al.* 2026).

Table 1. Statistical Criteria for Model Evaluation

Symbol	Criteria
Coefficient of determination (R^2)	$1-\frac{\sum_{i=1}^{n}(O_i-P_i)^2}{\sum_{i=1}^{n}(O_i-\bar{O})^2}$
Adjusted coefficient of determination (R^2_{adj})	$1-\frac{(n-1)(1-R^2)}{n-p}$
Mean squared error (MSE)	$\frac{1}{n}\sum_{i=1}^{n}(O_i-P_i)^2$
Mean absolute percentage error (MAPE)	$\frac{1}{n}\sum_{i=1}^{n}\lvert\frac{(P_i-O_i)}{P_i}\rvert 100$
Akaike information criterion (AIC)	$n\ln(\frac{SSE}{n})+2p$
	$SSE=\sum_{i=1}^{n}(O_i-P_i)^2$
Corrected Akaike information criterion (AICc)	$AIC+\frac{2p^2+2p}{n-p-1}$

RESULTS AND DISCUSSION

Fillers

Chemical composition

The chemical composition of the MS particles was analyzed to evaluate their potential as a lignocellulosic feedstock. The analysis revealed that MS is a cellulose-rich material, with an α-cellulose content of 45.7%. This value is comparable to various hardwoods, suggesting its suitability as a reinforcing filler in composites (Rangappa *et al.* 2022). The hemicellulose (15.9%) and lignin (25.5%) contents indicate a typical lignocellulosic structure. The extractives content was low (2.9%), which is advantageous for minimizing pitch deposition during industrial processing (Gao *et al.* 2024). The moisture content of the raw material was determined to be 19.0%. However, the ash content is relatively high (10.1%), a characteristic common in non-wood annual plants (Ferdous *et al.* 2020).

Fourier transform infrared spectroscopy

The FTIR spectrum of the MS particles is shown in Fig. 1. The absorbance axis was scaled to exclude atmospheric CO_2 interference (2300 to 2400 cm^{-1}) (Alalwan *et al.* 2023). A broad band at 3338 cm^{-1} was attributed to O–H stretching vibrations (Islam *et al.* 2023), confirming the fibers' highly hydrophilic nature due to abundant surface hydroxyl groups. Although the apparent intensity of this band was lower than some sharper absorption peaks, extensive hydrogen bonding within the lignocellulosic structure likely broadened the O–H absorption region and reduced its peak height. Peaks at 2914 cm^{-1} (C–H stretching) and 1370 cm^{-1} (C–H bending) corresponded to alkyl groups in cellulose and hemicelluloses (Belouadah *et al.* 2024; Thombare *et al.* 2023). The peak at 1749 cm^{-1} (C=O stretching) indicated the presence of hemicellulose and pectin, which contribute to water absorption (Stern 2025). A distinct peak at 1556 cm^{-1} corresponded to the aromatic skeletal

vibrations of lignin, a component that provides thermal stability and rigidity (Md Salim *et al.* 2021). Finally, a sharp peak at 1036 cm^{-1} was assigned to the C–O skeletal vibrations of the cellulose pyranose ring (Lou *et al.* 2025). This validated the high α-cellulose content (45.69%) determined *via* chemical analysis, confirming cellulose as the primary load-bearing component.

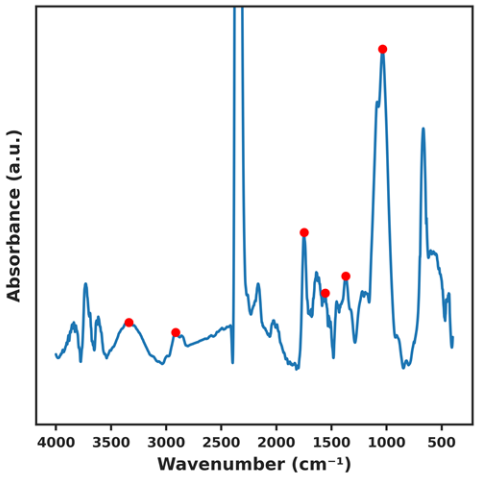

Fig. 1. FTIR spectrum of the MS filler

Scanning electron microscopy

Scanning electron microscopic (SEM) images (Fig. 2) revealed that the MS particles exhibited highly irregular shapes and a wide distribution of sizes. The micrographs highlighted a distinctly rough and highly textured surface morphology across the particles. While this inherent surface roughness is typically advantageous, as it increases the effective surface area available for physical mechanical interlocking with the polymer matrix, other morphological features might counteract this benefit. Specifically, the presence of localized voids and microcracks was observed over the particle surfaces, which could potentially act as failure initiation sites and decrease the overall mechanical performance of the composites when used as reinforcement. Furthermore, the sharp, angular corner points of these irregularly shaped particles might induce localized stress concentration areas within the polymer matrix under applied loads (Öncül and Sever 2025).

Mechanical Properties of Composites

Tensile tests

The tensile properties of PP and its composites are illustrated in Fig. 3. Incorporating MS particles into the PP matrix reduced the tensile strength by approximately 27.2%, dropping from 25.6 MPa for neat PP to 18.6 MPa for the 20MS2 formulation. Composites reinforced with MS1 exhibited relatively higher tensile strengths than those containing MS2. This overall reduction was attributed to poor interfacial adhesion between the hydrophilic fillers and the hydrophobic matrix (Khoo *et al.* 2025). Surface constituents, such as waxes and pectins, likely obscured reactive functional groups, preventing effective mechanical interlocking (Amiandamhen *et al.* 2020). Consequently, this insufficient adhesion led to extensive debonding and void formation, which acted as stress concentrators that negatively impacted the tensile strength (Olonisakin *et al.* 2022).

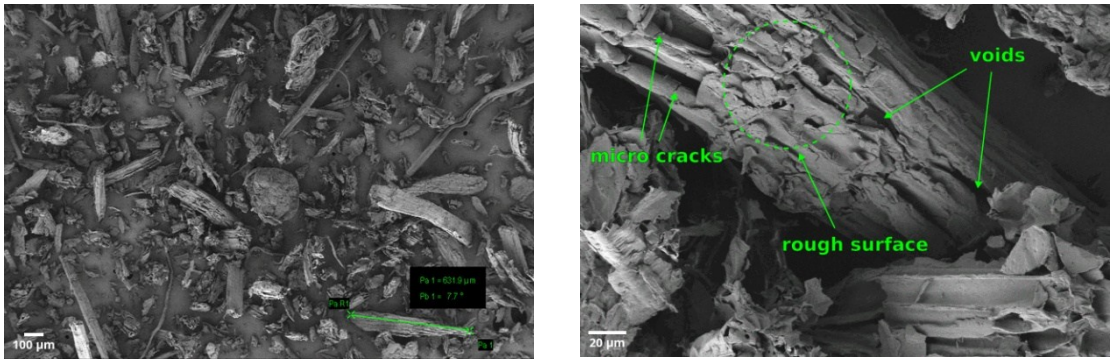

Fig. 2. SEM micrographs of the MS fillers: (a) low-magnification and (b) high-magnification images

The simultaneous observations from FTIR and SEM analyses provide further evidence for the reduction in tensile strength. FTIR spectra revealed no peak shifts or formation of new functional groups, indicating the absence of chemical interactions between the filler and matrix. Furthermore, SEM micrographs showed interfacial gaps and particle pull-out regions. These findings collectively suggest inefficient stress transfer across the interface, resulting in premature debonding under tensile loading.

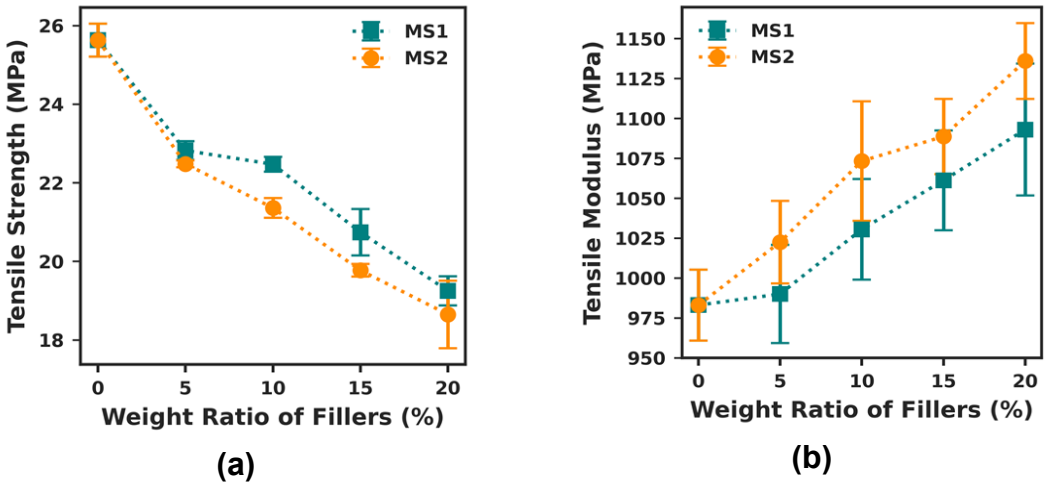

Fig. 3. Tensile test results, (a) tensile strength; and (b) tensile modulus

Conversely, the tensile modulus consistently increased with the addition of MS particles, reaching a maximum of 1140 MPa for the 20MS2 sample. This represented a 15.6% increase compared to the neat PP matrix (983 MPa). This enhanced stiffness is characteristic of particle-reinforced composites and was attributed to the rigid MS particles effectively restricting the mobility of the PP polymer chains near the fiber-matrix interface (Muniyadi *et al.* 2017; Wu *et al.* 2023; Öncül and Sever 2025).

Despite weak interfacial adhesion, the rigid lignocellulosic particles acted as mechanical constraints within the polymer matrix. The increased modulus indicates that stiffness enhancement was governed primarily by filler rigidity rather than interface quality. Similar behavior has frequently been reported in particulate PP composites where modulus is less sensitive to interfacial defects than strength (Wu *et al.* 2023; Öncül and Sever 2025).

Three point bending tests

The flexural properties of PP and its composites are presented in Fig. 4. Incorporating MS particles systematically decreased the flexural strength for both size fractions. Specifically, the addition of 20 wt% MS1 reduced the flexural strength by 29.6%, dropping from 43.71 MPa (neat PP) to 30.78 MPa. Although MS1 provided higher tensile strength, the MS2 composites exhibited relatively better flexural strength. This overall reduction was attributed to inefficient stress transfer caused by weak interfacial adhesion between the hydrophobic matrix and hydrophilic particles, which acted as defect sites leading to premature failure under flexural loading (Pęśko and Masek 2025).

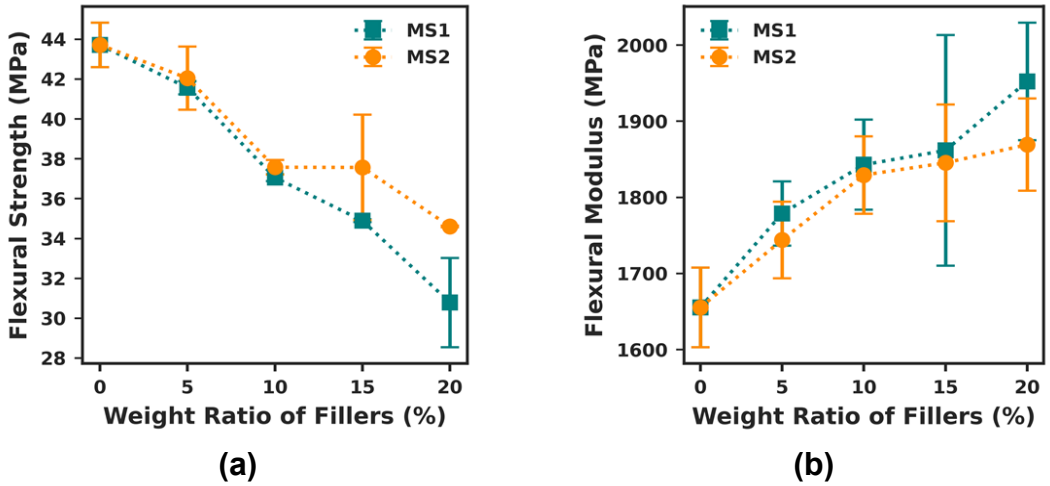

Fig. 4. Three point bending test results, (a) flexural strength; and (b) flexural modulus

Composites reinforced with MS1 exhibited higher modulus values compared to those with MS2. The maximum flexural modulus was recorded for the 20MS1 sample at 1952 MPa, representing an 18% increase compared to PP. This enhancement in stiffness suggests that despite the weak interfacial adhesion affecting strength, the presence of rigid fibers effectively restricted polymer chain mobility. Furthermore, the increase in modulus may be related to improved fiber-matrix interactions under the compressive stresses generated during bending (Hidalgo-Salazar and Salinas 2019). Under bending loads, larger particles may contribute to local resistance against compressive deformation on the compression side of the sample. Consequently, the influence of particle size on flexural strength differed from that observed under pure tensile loading.

Thermal Properties of Composites

Thermogravimetric analysis

Thermo-gravimetric analytic (TGA) curves of PP and its composites are presented in Fig. 5. The incorporation of MS particles significantly enhanced the thermal stability of the PP matrix. Neat PP exhibited the lowest thermal stability, with an onset degradation temperature (T_{onset}) of 410.0 °C and a maximum degradation temperature (T_{max}) of 443.0 °C. Upon the addition of MS particles, both the onset and maximum degradation temperatures shifted to considerably higher values across all loading levels. For instance, the T_{onset} for the composites ranged from 439.7 °C (for 5MS1) up to 444.9 °C (for 15MS1), while the T_{max} increased to a range between 461.5 °C (for 5MS1) and 463.2 °C (for

20MS2). Specifically, the addition of 20 wt% MS1 increased the T_{onset} by approximately 35 °C (to 444.7 °C) and the T_{max} by 20 °C (to 463.0 °C) compared to neat PP. A similar trend was observed for the MS2 samples, where the 20MS2 sample reached a T_{onset} of 444.8 °C and a T_{max} of 463.2 °C.

This improvement in thermal stability was attributed to the barrier effect mechanism. The lignocellulosic fillers, particularly their lignin and cellulose components, likely promoted the formation of a stable char layer that acted as a thermal insulator during thermal decomposition (Ornaghi *et al.* 2020). The weight loss data further verified the presence of inorganic material and char formation (Zhao *et al.* 2022). While PP degraded completely, exhibiting a 100.0% weight loss, all composite samples exhibited a residual mass. The total weight loss of the composites varied between 98.3% (for 10MS2) and 93.7% (for 20MS1). The weight loss generally decreased as fiber loading increased, indicating a higher char residue. The 20MS1 sample showed the lowest weight loss of 93.7%, implying a maximum char residue of approximately 6.3%.

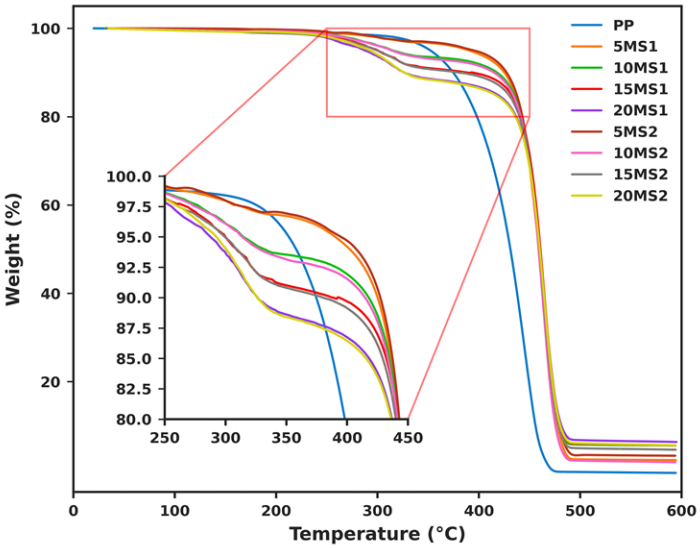

Fig. 5. TGA curves of PP and its composites

Differential scanning calorimetry

The melting and crystallization behaviors of PP and its composites were evaluated using DSC data (Table 2). The melting temperatures (T_m) remained relatively stable, ranging from 166.3 to 168.0 °C, indicating that the incorporation of MS particles did not significantly alter the crystal structure of the PP matrix. Similar observations have been reported for lignocellulosic filler-reinforced PP systems, where the filler primarily influences crystallization kinetics rather than crystal perfection or melting behavior (Belouadah *et al.* 2024; Jordà-Reolid *et al.* 2023).

The apparent melting enthalpy (ΔH_m) and crystallization enthalpy (ΔH_c) gradually decreased with increasing filler content. This behavior is commonly attributed to a dilution effect, whereby the relative amount of crystallizable PP decreases as the non-crystalline lignocellulosic fraction increases. Similar reductions in enthalpy values have been reported for PP composites reinforced with agricultural and wood-derived fillers (Jordà-Reolid *et al.* 2023; Bahlouli *et al.* 2023).

More pronounced changes were observed in the crystallization temperature (T_c). Neat PP exhibited a T_c value of 121.1 °C, whereas most composite formulations showed higher crystallization temperatures, reaching 123.8 °C for the 15MS2 sample. This behavior suggests that the MS particles acted as heterogeneous nucleating agents. The hydroxyl-rich lignocellulosic surfaces provided energetically favorable sites for crystal nucleation, thereby reducing the energy barrier required for crystal formation and promoting crystallization at higher temperatures. Similar nucleating effects have been widely reported in natural fiber-reinforced PP composites (Sever *et al.* 2019; Wu *et al.* 2023; Öncül and Sever 2025).

However, at the highest filler loading, particularly for the 20MS1 formulation, the crystallization temperature decreased to 119.1 °C. This reduction can be attributed to particle agglomeration and restricted polymer chain mobility. Excessive filler loading may reduce the available space for crystal growth and hinder molecular diffusion, thereby delaying crystallization despite the presence of additional nucleation sites. Similar competing nucleation and mobility-restriction mechanisms have been reported in highly filled lignocellulosic polymer composites (Belouadah *et al.* 2024; Bahlouli *et al.* 2023).

Although the crystallization temperature was affected by filler incorporation, the degree of crystallinity remained within a relatively narrow range. This observation indicates that MS particles primarily influenced the kinetics of crystallization rather than the final crystalline content. The DSC findings also help explain the mechanical behavior of the composites. The increase in stiffness observed in tensile and flexural modulus measurements may be partially attributed to the earlier crystallization and localized ordering induced by the filler particles. Similar relationships between lignocellulosic filler incorporation, restricted polymer chain mobility, and stiffness enhancement have been reported for PP-based composites (Öncül and Sever 2025).

Table 2. Melting and Crystallization Parameters of the Samples

Sample	T_m (°C)	T_c (°C)	H_c (J/g)	H_m (J/g)	X_c (%)
PP	168.0485	121.0846	92.42	89.83	43.4
5MS1	167.0011	123.2872	86.8	85.35	41.23
10MS1	167.5399	122.1121	82.4	80.74	39
15MS1	166.8666	119.7619	77.38	78.45	37.9
20MS1	166.6116	119.0703	71.73	74.93	36.2
5MS2	166.4203	120.883	82.58	83.65	40.41
10MS2	166.3407	123.0344	80.48	82.82	40.01
15MS2	167.6952	123.8167	77	78.62	37.98
20MS2	167.0144	122.9314	71.37	71.83	34.7

Chemical and Morphological Characterization of Composites

Fourier-transform infrared spectroscopy

The spectrum of the PP matrix displayed characteristic aliphatic signatures at 2935.8 cm^{-1} (asymmetric and symmetric C–H stretching) (Belouadah *et al.* 2024), along with strong peaks at 1454.4 cm^{-1} and 1377.2 cm^{-1} (C–H and $–CH_3$ bending vibrations) (Verma and Meena 2025; Myung *et al.* 2026). Upon incorporating MS particles, new absorbance bands associated with lignocellulosic components emerged proportionally with fiber loading (Fig. 6). Specifically, the heavily loaded 20MS1 composite exhibited a broad hydroxyl peak at 3418.0 cm^{-1} (O–H stretching of cellulose and moisture) (Islam *et al.* 2023), a carbonyl band at 1645.3 cm^{-1} (C=O stretching of hemicellulose or absorbed water) (Oudir *et al.* 2023), a lignin-associated peak at 1556.6 cm^{-1} (aromatic skeletal vibrations)

(Helal *et al.* 2023), and a polysaccharide signature at 1047.4 cm^{-1} (pyranose ring stretching vibrations) (Lou *et al.* 2025).

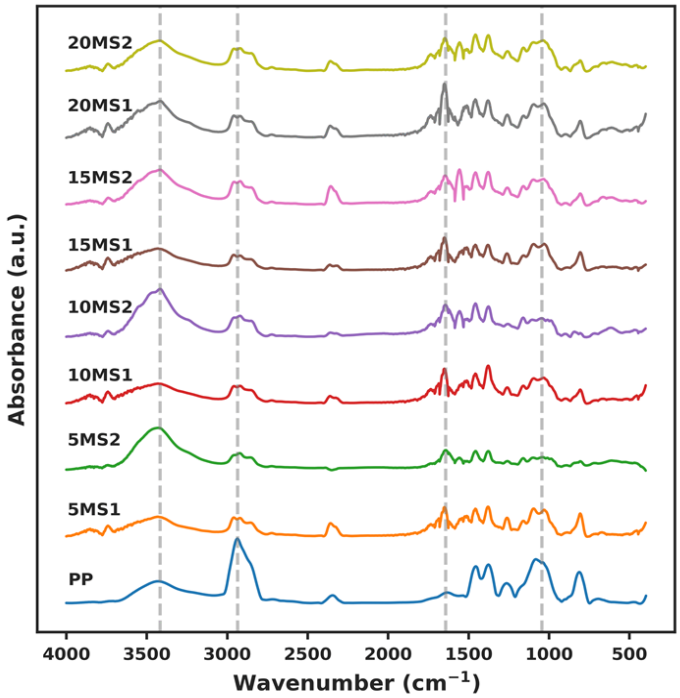

Fig. 6. FTIR spectra of the PP and its composites

Crucially, the comparative analysis revealed no peak shifts or the formation of new functional groups, indicating the absence of covalent linkages at the fiber-matrix interface. The composite spectra were effectively superpositions of the neat PP and raw MS signatures. This lack of chemical interaction confirmed a pronounced polarity mismatch between the highly hydrophilic, hydroxyl-rich MS particles and the strictly hydrophobic PP matrix. Consequently, interfacial interactions were restricted to weak physical entanglements, which explained the interfacial debonding and fiber pull-out observed during mechanical testing. However, the presence of the rigid cellulose structure and aromatic lignin rings successfully accounted for the enhanced thermal stability of the overall composites.

Scanning electron microscopy

The fracture surface morphologies of the composite samples are presented in Fig. 7. The fracture surfaces exhibited distinct micro-gaps and voids between the lignocellulosic particles and the PP matrix. These features indicated incomplete interfacial contact and poor interfacial compatibility resulting from the polarity mismatch between the hydrophilic filler and the hydrophobic polymer matrix (Yuan *et al.* 2025). The presence of interfacial gaps suggests that effective stress transfer could not be established throughout the composite structure (Öncül 2023). Consequently, particle debonding and pull-out occurred under loading, contributing to the reduction in tensile and flexural strengths.

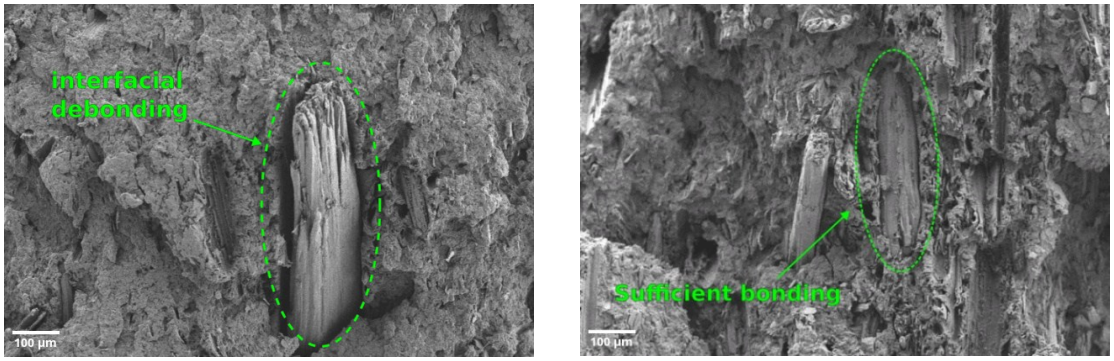

(a) (b)

Fig. 7. SEM micrographs: (a) interfacial debonding and gaps, and (b) filler–matrix contact regions

Mathematical Modeling of Mechanical Properties

Tensile test results

The predictive models obtained for tensile strength and tensile modulus using the three different regression-based response surface techniques (SR, FSR, and BER) are summarized in Table 3. A significant outcome of the modeling process was that all three regression approaches converged to identical final models for both response parameters, yielding the same model structure and coefficient values. This result indicated a strong and consistent statistical relationship between the design variables and the tensile responses. It also demonstrated the robustness of the model selection process regardless of the regression strategy employed.

Table 3. Proposed Mathematical Model for Tensile Strength and Tensile Modulus and their Prediction Performance

Property	Method	Model	R^2	R^2_{adj}	MSE	MAPE	AICc
Tensile Strength	SR FSR BER	$Y = 25.503 - 0.2615\ x_1 - 0.850\ x_2$	0.985	0.980	0.062	0.833	11.297
Tensile Modulus	SR FSR BER	$Y = 983.01 + 6.954\ x_1 - 57.7\ x_2 + 31.36\ x_2^2$	0.987	0.983	29.049	0.388	73.862

In the tensile strength model, the negative coefficients associated with both variables indicated that an increase in particle infill ratio or particle size tended to reduce the tensile strength of the composite. Among the two parameters, particle size exhibited a stronger influence because of its larger coefficient magnitude. The statistical performance indicators further confirmed the reliability of the developed model. The R^2 and R^2adj values indicated that approximately 98% of the variability in tensile strength was explained by the regression model. In addition, the extremely low MSE (0.062) and MAPE (0.833%) values suggested that prediction deviations from the experimental values were minimal. The AICc value of 11.297, which penalizes model complexity while rewarding goodness of fit, also supported the adequacy of the selected model.

The ANOVA results provided in Table 4 for tensile strength offered further statistical validation. The regression model accounted for 98.51% of the total variation, indicating that the proposed predictors effectively captured the behavior of the response variable. Specifically, the particle infill ratio contributed 92.17% to the total variation and

exhibited the highest F-value (235.44), demonstrating that it was the dominant factor influencing tensile strength. In contrast, particle size contributed 6.34%, indicating a secondary but still statistically significant effect. The relatively small error contribution (1.49%) confirmed the high predictive capability of the model.

Table 4. ANOVA Results for Tensile Strength

Source	DF	Seq SS	Contribution	Adj SS	Adj MS	F-Value	P-Value
Regression	2	36.9067	98.51%	36.9067	18.4534	198.82	0
x_1	1	34.5316	92.17%	21.8523	21.8523	235.44	0
x_2	1	2.3751	6.34%	2.3751	2.3751	25.59	0.002
Error	6	0.5569	1.49%	0.5569	0.0928		
Total	8	37.4636	100.00%				

Unlike tensile strength, the tensile modulus model included a quadratic term for particle size (x_2^2), indicating a non-linear relationship between particle size and modulus. The positive coefficient of x_1 suggested that increasing the particle infill ratio enhanced the tensile modulus, while the negative linear coefficient of x_2 indicated an initial decrease in modulus with increasing particle size. However, the presence of the positive quadratic term implied that the effect of particle size was non-linear and exhibited curvature across the design space. The predictive performance of the tensile modulus model was highly satisfactory; R^2 and R^2adj values of 0.987 and 0.983, respectively, indicated that nearly 99% of the variation was explained by the model (Table 5).

The adequacy of the developed regression models for both tensile parameters was further evaluated through graphical diagnostic tools (Fig. 8). The normal probability plots showed that the standardized residuals were closely aligned with the reference straight line, satisfying the regression assumptions regarding error normality. Furthermore, the histograms of standardized residuals exhibited a symmetric distribution around zero without noticeable skewness, and the residuals versus observation order plots fluctuated randomly, confirming the absence of systematic bias.

Table 5. ANOVA Results for Tensile Modulus

Source	DF	Seq SS	Contribution	Adj SS	Adj MS	F-Value	P-Value
Regression	3	20273	98.73%	20273	6757.7	129.27	0
x_1	1	17579.7	85.61%	12089.2	12089.2	231.26	0
x_2	1	1324.6	6.45%	704.3	704.3	13.47	0.014
x_2^2	1	1368.7	6.67%	1368.7	1368.7	26.18	0.004
Error	5	261.4	1.27%	261.4	52.3		
Total	8	20534.4	100.00%				

The effects of the design parameters on the tensile responses were visualized through contour and 3D response surface plots (Fig. 8). For tensile strength, the contour map revealed a clear gradient along both design variables, demonstrating that increasing either the particle infill ratio or the particle size led to a reduction in tensile strength. The corresponding 3D response surface plot confirmed this trend with a nearly planar, downward-sloping surface. For tensile modulus, the 3D surface illustrated that the modulus generally increased with the particle infill ratio, while the influence of particle size exhibited a curvature indicative of the quadratic effect.

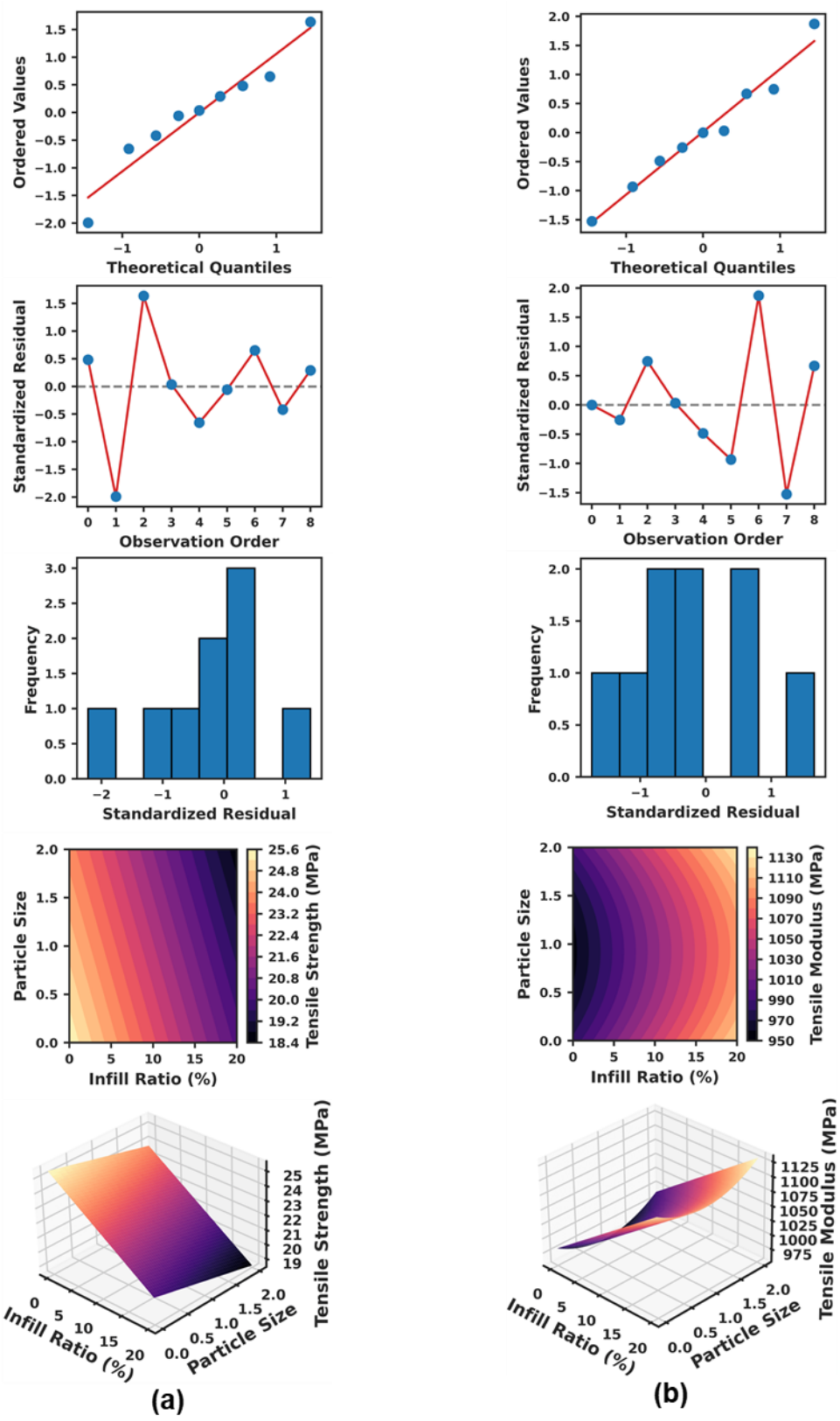

Fig. 8. Graphical evaluation of the regression models for (a) tensile strength and (b) tensile modulus

Three point bending results

Unlike the tensile responses, where all three methods converged to identical models, the bending responses showed different model structures depending on the regression technique used (Table 6). This divergence indicated that the relationship between the design variables and the flexural responses was slightly more complex.

Table 6. Proposed Mathematical Models for Flexural Strength and Flexural Modulus and their Prediction Performance

Property	Method	Model	R^2	R^2_{adj}	MSE	MAPE	AICc
Flexural Strength	SR FSR BER	$Y = 43.964 - 0.807\ x_1 - 0.029\ x_2 + 0.1673\ x_1 x_2$	0.985	0.980	0.062	0.833	11.297
Flexural Modulus	SR	$Y = 1694.5 + 11.27\ x_1$	0.859	0.813	897.082	1.434	92.733
	FSR	$Y = 1659.3 + 22.63x_1 + 18.1x_2 - 0.275\ x_1^2 - 4.17\ x_1 x_2$	0.963	0.950	238.109	0.692	104.795
	BER	$Y = 1655.3 + 9.31\ x_1 + 149.1\ x_2 - 62.0\ x_2^2$	0.954	0.938	295.083	0.74	94.726

For flexural strength, a notable finding was that all three modeling techniques converged to the same regression equation. The model included linear terms of the design variables and an interaction term between particle infill ratio and particle size. The model performance indicators showed strong predictive capability, explaining approximately 98% of the variation in flexural strength. The ANOVA results for flexural strength (Table 7) confirmed that the regression term accounted for 96.44% of the total variation. Among the predictors, the particle infill ratio was the dominant factor, contributing 88.88% of the total variability, while the interaction term contributed 3.81% and approached statistical significance.

Table 7. ANOVA Results for Flexural Strength.

Source	DF	Seq SS	Contribution	Adj SS	Adj MS	F-Value	P-Value
Regression	3	130.857	96.44%	130.857	43.619	45.19	0
x_1	1	120.597	88.88%	61.451	61.4513	63.66	0
x_2	1	5.086	3.75%	0.001	0.0014	0	0.971
$x_1 x_2$	1	5.174	3.81%	5.174	5.1745	5.36	0.068
Error	5	4.826	3.56%	4.826	0.9653		
Total	8	135.683	100.00%				

For flexural modulus, the regression models differed more noticeably among the three selection methods. The SR model produced a relatively simple linear relationship dominated by the particle infill ratio, whereas the FSR and BER models introduced additional terms, including quadratic and interaction effects. To identify the most reliable predictive model among the variations, a heat map analysis was performed based on a normalized scoring system across all evaluation criteria (Fig. 9).

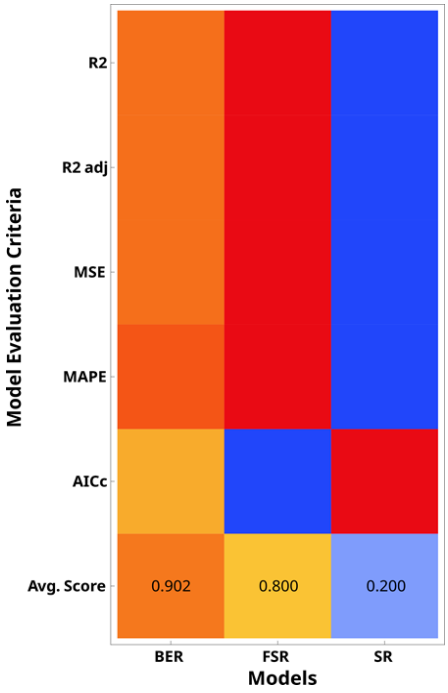

Fig. 9. Heat map analysis of the model evaluation criteria for flexural modulus

As illustrated in Fig. 9, the BER method emerged as the superior approach for flexural modulus, achieving the highest average success score of 0.902. While the FSR method showed a high R^2 (0.963), the BER model provided a more balanced performance, particularly with a superior (lower) AICc value of 94.726 compared to FSR's 104.795, suggesting better model parsimony. Consequently, the BER-derived model was recommended for characterizing the flexural modulus. The ANOVA results for the flexural modulus (Table 8) supported this, demonstrating that the influence of particle size was primarily non-linear, as the quadratic term (x_2^2) contributed 9.31% to the variance.

Table 8. ANOVA Results for Flexural Modulus

Source	DF	Seq SS	Contribution	Adj SS	Adj MS	F-Value	P-Value
Regression	3	54769.3	95.38%	54769	18256.4	34.37	0.001
x_1	1	49351.2	85.94%	21647	21646.7	40.76	0.001
x_2	1	69.2	0.12%	4709	4709.3	8.87	0.031
x_2^2	1	5348.8	9.31%	5349	5348.8	10.07	0.025
Error	5	2655.7	4.62%	2656	531.1		
Total	8	57424.9	100.00%				

The statistical reliability of the flexural regression models was verified through graphical diagnostic tools, showing residuals that satisfied normality assumptions without systematic bias (Fig. 10). Regarding the mechanical response visualizations, the flexural strength contour and 3D surface plots displayed a nearly flat, tilted surface indicating a clear linear decrease in resistance as parameters increased.
and stress raisers rather than load-bearing elements.

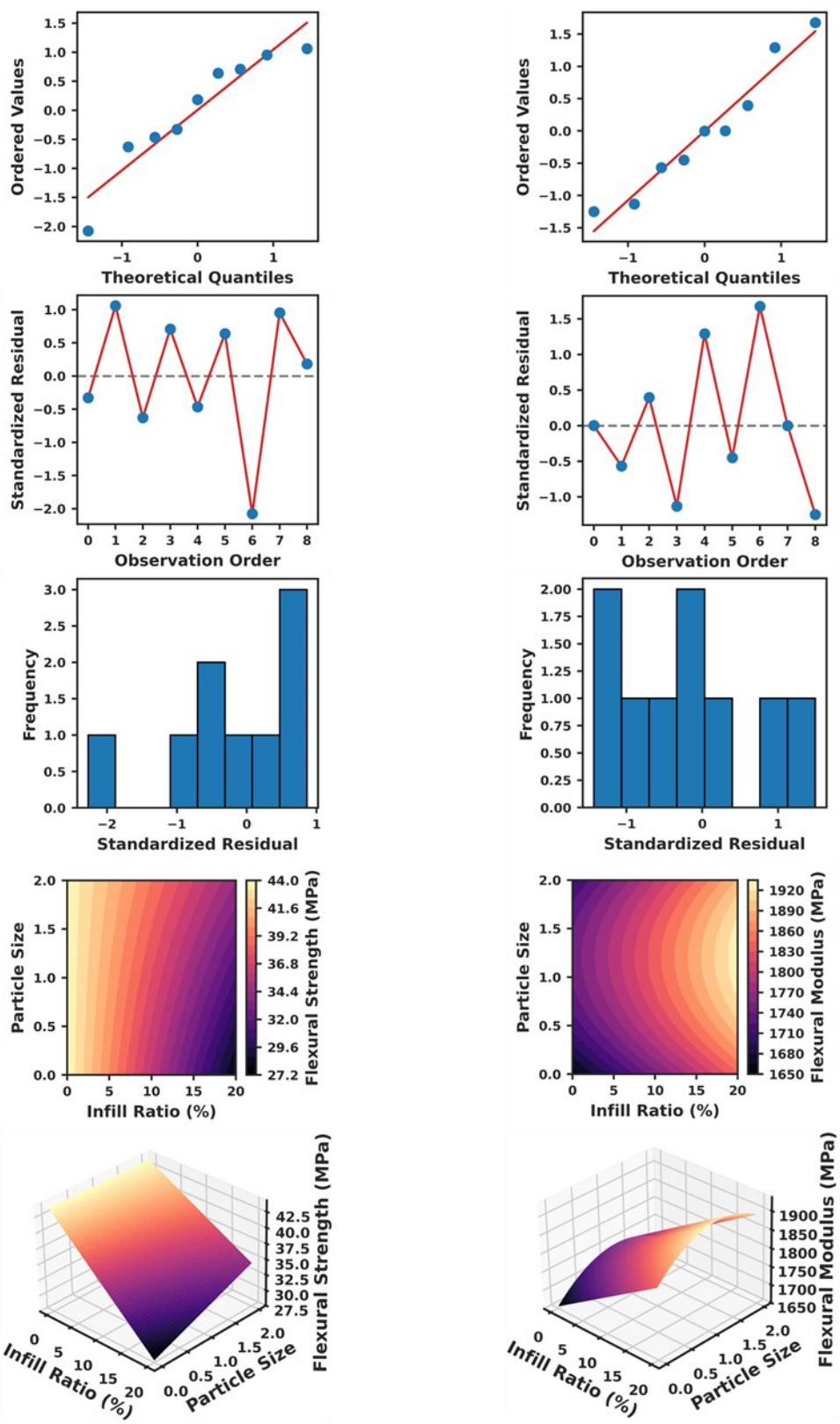

Fig. 10. Graphical evaluation of the regression models for (a) flexural strength; and (b) flexural modulus

Unlike strength, the flexural modulus exhibited a non-linear response; the curvature in the 3D surface, particularly along the x_2 axis, visually confirmed the strong quadratic effects mathematically identified in the BER model.

While the experiment provides a direct assessment of the composites' performance, the mathematical modeling process offers a deeper validation of these phenomena. In the mathematical modeling process, the retention or systematic exclusion of specific terms serves as a direct mathematical diagnostic tool, explicitly revealing the phase incompatibility, localized defect density, and the lack of interfacial bonding between the hydrophobic PP matrix and the hydrophilic MS bio-particles. In this study, the mathematical frameworks derived from the response surface techniques offer substantial microstructural insights, specifically elucidating the thermodynamic incompatibility and poor interfacial contact between the uncoupled phases. In the elastic region, the Tensile Modulus model retains a statistically significant positive quadratic term for particle size ($+31.36x_2^2$), while the Flexural Modulus models diverge into non-linear architectures incorporating negative interaction and higher-order terms (such as $-4.17x_1x_2$ and $-62.0x_2^2$). These non-linear curvatures across the design space mathematically signify that the elastic stress-transfer mechanism shifts dynamically as a function of filler loading and dimensions. Due to the poor interfacial adhesion between the PP matrix and MS fibers, higher filler concentrations and larger dimensions inevitably promote particle clustering and local stress fields, forcing the regression systems to retain higher-order parameters to maintain predictive accuracy ($R^2 > 0.95$). Conversely, at the ultimate failure threshold, the systematic elimination of higher-order terms in the Tensile Strength model resulting in a strictly linear degradation equation ($Y = 25.503 - 0.2615x_1 - 0.850x_2$) shows that the uncoupled bio-particles act strictly as mechanical discontinuities

The mathematical parameters governing the ultimate strength models serve as a direct diagnostic tool for assessing the interfacial contact quality of the composites. The developed Tensile Strength model, characterized by exclusively negative linear terms, registers continuous mechanical degradation across the entire design space. The rigorous exclusion of any positive quadratic or synergetic interaction parameters during the mathematical selection process indicates that the filler phase functions exclusively as a structural defect under macro-deformation. Without chemical bonding to bridge the hydrophobic-hydrophilic interface, the applied tensile load cannot be transferred from the ductile PP matrix to the rigid composites, thereby driving the linear reduction in strength as the filler volume fraction grows. Under flexural loading, the poor interfacial bonding manifests as a distinctive cross-product interaction term ($+0.1673x_1x_2$). Because three-point bending induces severe interlaminar shear stress, the lack of adhesion prompts micro-separation along the interface. The positive sign of this interaction term mathematically denotes that the magnitude of strength degradation is highly dependent on the total interfacial contact area, where smaller particle sizes maximize the density of unbonded boundary layers, whereas larger dimensions restrict the local shear failure paths. Thus, the empirical structure of both strength models strongly substantiates the physical presence of poor interfacial contact. Consequently, the empirical model terms selection process and the development of mathematical models through various modeling methods yield effective and consistent insights into interfacial contact and the nature of phase incompatibility.

CONCLUSIONS

1. Polypropylene (PP) composites reinforced with *Malva sylvestris* L. (MS) particles were successfully produced using thermokinetic mixing and compression molding. The results demonstrated that MS is a viable lignocellulosic filler for PP-based composite applications.
2. Increasing the filler content reduced the tensile and flexural strengths by up to 27.2% and 29.6%, respectively. In contrast, the tensile and flexural moduli increased by up to 15.6% and 18.0%, respectively, demonstrating improved composite stiffness.
3. The incorporation of MS particles enhanced the thermal stability of PP, increasing the onset degradation temperature by approximately 35 °C at 20 wt% filler loading. The particles also influenced the crystallization behavior of the matrix while maintaining a comparable degree of crystallinity.
4. Response Surface Methodology (RSM) successfully modeled the mechanical properties of the composites. Linear model provided the best predictions for tensile strength, whereas quadratic models yielded higher predictive accuracy for tensile modulus and flexural properties. Among the evaluated approaches, backward elimination produced the most effective model for flexural modulus prediction.

ACKNOWLEDGMENTS

The authors acknowledge funding from Izmir Katip Celebi University (Grant #2025-TYL-FEBE-0035) and from the Scientific and Technological Research Council of Türkiye (TÜBİTAK) (Grant #1139B412101860).

REFERENCES CITED

Abraha, K. G., Debeli, D. K., Ghani, M. U., Tesfahunegn, A. A., and Guo, J. (2023). "Enet fiber-reinforced polylactic acid-based biocomposites for high-performance application," *J. Compos. Sci.* 7(10), article 407. https://doi.org/10.3390/jcs7100407

Alalwan, H. A., Alminshid, A., Mohammed, M. M., and Mohammed, M. F. (2023). "Spectroscopic investigation of carbon dioxide interactions with transition metal-oxide nanoparticles," *Chem. Eng. Technol.* 46(3), 587-594. https://doi.org/10.1002/ceat.202200250

Amiandamhen, S. O., Meincken, M., and Tyhoda, L. (2020). "Natural fibre modification and its influence on fibre-matrix interfacial properties in biocomposite materials," *Fibers Polym.* 21(4), 677-689. https://doi.org/10.1007/s12221-020-9362-5

ASTM D638-22. (2022). "Standard test method for tensile properties of plastics," ASTM International, West Conshohocken, PA. https://doi.org/10.1520/D0638-22

ASTM D790-17. (2017). "Standard test methods for flexural properties of unreinforced and reinforced plastics and electrical insulating materials," ASTM International, West Conshohocken, PA. https://doi.org/10.1520/D0790-17

Bahlouli, S., Belaadi, A., Makhlouf, A., Alshahrani, H., Khan, M. K. A., and Jawaid, M. (2023). "Effect of fiber loading on thermal properties of cellulosic Washingtonia reinforced HDPE biocomposites," *Polymers* 15(13), article 2910. https://doi.org/10.3390/polym15132910

Belouadah, Z., Nasri, K., and Toubal, L. (2024). "The effects of lignin on the thermal and morphological properties and damage mechanisms after UV irradiation of polypropylene biocomposites reinforced with flax and pine fibres: Acoustic emission analysis," *Materials* 17(11), article 2474. https://doi.org/10.3390/ma17112474

Bharath, K. N., and Basavarajappa, S. (2016). "Applications of biocomposite materials based on natural fibers from renewable resources: A review," *Sci. Eng. Compos. Mater.* 23(2), 123-133. https://doi.org/10.1515/secm-2014-0088

Diambu, A. N., and Çevik, M. (2025). "Extraction and comprehensive characterization of novel *Encephalartos ituriensis* fiber for biocomposite reinforcement," *Cellulose* 32(15), 9061-9084. https://doi.org/10.1007/s10570-025-06750-1

Ferdous, T., Jahan, M. S., Quaiyyum, M. A., and Uddin, M. N. (2020). "Formic acid pulping of crops residues available in Bangladesh," *Biomass Convers. Biorefin.* 10(2), 289-297. https://doi.org/10.1007/s13399-019-00415-3

Gao, C., Cui, X., and Matsumura, J. (2024). "Multidimensional exploration of wood extractives: A review of compositional analysis, decay resistance, light stability, and staining applications," *Forests* 15(10), article 1782. https://doi.org/10.3390/f15101782

Helal, M. I. D., Tong, Z., Khater, H. A., Fathy, M. A., Ibrahim, F. E., Li, Y., and Abdelkader, N. H. (2023). "Modification of fabrication process for prolonged nitrogen release of lignin–montmorillonite biocomposite encapsulated urea," *Nanomaterials* 13(12), article 1889. https://doi.org/10.3390/nano13121889

Hidalgo-Salazar, M. A., and Salinas, E. (2019). "Mechanical, thermal, viscoelastic performance and product application of PP-rice husk Colombian biocomposites," *Compos. Part B Eng.* 176, article 107135. https://doi.org/10.1016/j.compositesb.2019.107135

Hossain, Md. T., Shahid, Md. A., Mahmud, N., Habib, A., Rana, Md. M., Khan, S. A., and Hossain, Md. D. (2024). "Research and application of polypropylene: A review," *Discover Nano* 19(1), 2. https://doi.org/10.1186/s11671-023-03952-z

Islam, R., Noyon, M. A. R., Dey, T. K., Jamal, M., Rathanasamy, R., Chinnasamy, M., and Uddin, Md. E. (2023). "Fabrication of graphene oxide reinforced biocomposite: Recycling of postconsumed footwear leather," *Adv. Polym. Technol.* 2023, 1-10. https://doi.org/10.1155/2023/3996687

Jordà-Reolid, M., Moreno, V., Martínez-Garcia, A., Covas, J. A., Gomez-Caturla, J., Ivorra-Martinez, J., and Quiles-Carrillo, L. (2023). "Incorporation of argan shell flour in a biobased polypropylene matrix for the development of high environmentally friendly composites by injection molding," *Polymers* 15(12), article 2743. https://doi.org/10.3390/polym15122743

Karasulu, D. C., Öncül, M., Özcan, O., and Sütçü, M. (2026). "Performance evaluation of lignocellulosic fiber-reinforced brake pads using hybrid optimization techniques," *Polym. Compos.* 47(8), 7657-7674. https://doi.org/10.1002/pc.70648

Khoo, P. S., Rizal, M. A. M., Yajid, M. A. M., Hassan, S. A., Yahya, M. Y., and Wahit, M. U. (2025). "Unveiling favorable mechanical properties of lignocellulosic wood–reinforced thermoplastic composites as future green and sustainable materials," *Fibers Polym.* 26(4), 1425-1448. https://doi.org/10.1007/s12221-025-00874-8

Lou, J., Dong, A., and Hu, L. (2025). "A readily degradable polyvinyl alcohol/starch membrane containing catechol-grafted microcrystalline cellulose for preserving fruit freshness," *Appl. Biochem. Biotechnol.* 197(9), 5714-5732. https://doi.org/10.1007/s12010-025-05321-1

Md Salim, R., Asik, J., and Sarjadi, M. S. (2021). "Chemical functional groups of extractives, cellulose and lignin extracted from native *Leucaena leucocephala* bark," *Wood Sci. Technol.* 55(2), 295-313. https://doi.org/10.1007/s00226-020-01258-2

Modesti, M., Lorenzetti, A., Bon, D., and Besco, S. (2006). "Thermal behaviour of compatibilised polypropylene nanocomposite: Effect of processing conditions," *Polym. Degrad. Stab.* 91(4), 672-680. https://doi.org/10.1016/j.polymdegradstab.2005.05.018

Muniyadi, M., Yit Siew Ng, T., Munusamy, Y., and Ooi, Z. X. (2017). "*Mimusops elengi* seed shell powder as a new bio-filler for polypropylene-based bio-composites," *BioResources* 13(1), 272-289. https://doi.org/10.15376/biores.13.1.272-289

Myung, J. H., Kim, C. Y., and Yu, W.-R. (2026). "Fabrication of PEDOT:PSS shape memory polymer composites using vertical phase separation by surface energy," *Smart Mater. Struct.* 35(1), article 015052. https://doi.org/10.1088/1361-665X/ae3928

Nascimento, L. F. C., Holanda, L. I. F., Louro, L. H. L., Monteiro, S. N., Gomes, A. V., and Lima Júnior, É. P. (2017). "Evaluation of ballistic armor behavior with epoxy composite reinforced with malva fibers," in: *Characterization of Minerals, Metals, and Materials 2017*, Springer, pp. 647-655. https://doi.org/10.1007/978-3-319-51382-9_71

Olonisakin, K., Fan, M., Zhang, X.-X., Ran, L., Lin, W., Zhang, W., and Yang, W. (2022). "Key improvements in interfacial adhesion and dispersion of fibers/fillers in polymer matrix composites; Focus on PLA matrix composites," *Compos. Interfaces* 29(10), 1071-1120. https://doi.org/10.1080/09276440.2021.1878441

Öncül, M. (2023). *Influence of Lignocellulosic Fillers and Interfaces on Thermal and Mechanical Properties of Biocomposites*, Ph.D. Dissertation, Izmir Katip Celebi University, Izmir, Türkiye. https://acikerisim.ikcu.edu.tr/yayin/1742488

Öncül, M. (2026). "Experimental–numerical framework for evaluating the mechanical response of *Cornus sanguinea* L.-reinforced polypropylene biocomposites," *Polymers* 18(9), article 1020. https://doi.org/10.3390/polym18091020

Öncül, M., Atagür, M., Atan, E., and Sever, K. (2025). "A preliminary evaluation of bing cherry tree (*Prunus avium* L.) pruning waste as an alternative lignocellulosic filler for lightweight composite material applications," *Polym. Compos.* 46(4), 3655-3667. https://doi.org/10.1002/pc.29197

Öncül, M., and Sever, K. (2025). "Effect of particle size and loading of cherry tree branch fillers on the mechanical and viscoelastic properties of polypropylene composites," *BioResources* 20(1), 1703-1712. https://doi.org/10.15376/biores.20.1.1703-1712

Ornaghi, H. L., Ornaghi, F. G., Neves, R. M., Monticeli, F., and Bianchi, O. (2020). "Mechanisms involved in thermal degradation of lignocellulosic fibers: A survey based on chemical composition," *Cellulose* 27(9), 4949-4961. https://doi.org/10.1007/s10570-020-03132-7

Oudir, M., Ait Mesbah, Z., Lerari, D., Issad, N., and Djenane, D. (2023). "Development of eco-friendly biocomposite films based on *Opuntia ficus-indica* cladodes powder

blended with gum arabic and xanthan envisaging food packaging applications," *Foods* 13(1), article 78. https://doi.org/10.3390/foods13010078

Özçiçek, İ. B., Aydin, L., and Savran, M. (2026). "A new advanced design-modeling-optimization procedure for pulsed metal inert gas welding using hybrid multiple non-linear neuro-regression and stochastic search methods," *Weld. World* 70(1), 167-185. https://doi.org/10.1007/s40194-025-02182-4

Pęśko, M., and Masek, A. (2025). "Plant-based biofillers for polymer composites: Characterization, surface modification, and application potential," *Polymers* 17(17), article 2286. https://doi.org/10.3390/polym17172286

Pokharel, A., Falua, K. J., Babaei-Ghazvini, A., and Acharya, B. (2022). "Biobased polymer composites: A review," *J. Compos. Sci.* 6(9), article 255. https://doi.org/10.3390/jcs6090255

Rangappa, S. M., Siengchin, S., Parameswaranpillai, J., Jawaid, M., and Ozbakkaloglu, T. (2022). "Lignocellulosic fiber reinforced composites: Progress, performance, properties, applications, and future perspectives," *Polym. Compos.* 43(2), 645-691. https://doi.org/10.1002/pc.26413

Savran, M. (2026). "Experimental analysis and a novel stepwise nonlinear hybrid ANN-based machine learning approach for optimizing the mechanical and surface performance of 3D-printed PLA," *Measurement* 259, article 119648. https://doi.org/10.1016/j.measurement.2025.119648

Savran, M., and Aydin, L. (2024). *An Integrated Approach to Modeling and Optimization in Engineering and Science* (1st Ed.), CRC Press. https://doi.org/10.1201/9781003494843

Savran, M., Öncül, M., Yılmaz, M., Aydın, L., and Sever, K. (2023). "Modeling and optimization of dynamic-mechanical properties of hybrid polymer composites by multiple nonlinear neuro-regression method," *Sigma J. Eng. Nat. Sci.* 41(6), 1243-1254. https://doi.org/10.14744/sigma.2023.00143

Sever, K., Atagür, M., Tunçalp, M., Altay, L., Seki, Y., and Sarıkanat, M. (2019). "The effect of pumice powder on mechanical and thermal properties of polypropylene," *J. Thermoplast. Compos. Mater.* 32(8), 1092-1106. https://doi.org/10.1177/0892705718785692

Stern, T. (2025). "Deciphering the triple-peak C-O-C stretching FTIR absorbance consistently occurring in semicrystalline PEG," *Polymers* 17(16), article 2199. https://doi.org/10.3390/polym17162199

TAPPI. (1999). "Alpha-, beta- and gamma-cellulose in pulp," TAPPI Test Method T 203 cm-99, Technical Association of the Pulp and Paper Industry, Atlanta, GA.

TAPPI. (2002). "Ash in wood, pulp, paper and paperboard: Combustion at 525 °C," TAPPI Test Method T 211 om-02, Technical Association of the Pulp and Paper Industry, Atlanta, GA.

TAPPI. (2006). "Acid-insoluble lignin in wood and pulp," TAPPI Test Method T 222 om-02, Technical Association of the Pulp and Paper Industry, Atlanta, GA.

TAPPI. (2007). "Solvent extractives of wood and pulp," TAPPI Test Method T 204 cm-97, Technical Association of the Pulp and Paper Industry, Atlanta, GA.

Thombare, N., Mahto, A., Singh, D., Chowdhury, A. R., and Ansari, M. F. (2023). "Comparative FTIR characterization of various natural gums: A criterion for their identification," *J. Polym. Environ.* 31(8), 3372-3380. https://doi.org/10.1007/s10924-023-02821-1

Verma, V., and Meena, J. (2025). "Synthesis, characterization, and application of a novel carboxymethyl guar gum/zinc oxide (CMGG/ZnO) nano biocomposite for methylene blue dye adsorption," *ChemistrySelect* 10(30), article e02324. https://doi.org/10.1002/slct.202502324

Wu, Q., Liu, C., Li, S., Yan, Y., Yu, S., and Huang, L. (2023). "Micronized cellulose particles from mechanical treatment and their performance on reinforcing polypropylene composite," *Cellulose* 30(1), 235-246. https://doi.org/10.1007/s10570-022-04905-y

Yuan, F., Li, Q., Yu, T., Zhou, J., and Li, Y. (2025). "Continuous high-efficiency treatment and process optimization of pultruded plant fiber reinforced composites for structural applications," *Polym. Compos.* pc.70713. https://doi.org/10.1002/pc.70713

Zhao, X., Oyedeji, O., Webb, E., Wasti, S., Bhagia, S., Hinton, H., Li, K., Kim, K., Wang, Y., Zhu, H., Vaidya, U., Labbé, N., Tekinalp, H., Gallego, N. C., Pu, Y., Ragauskas, A. J., and Ozcan, S. (2022). "Impact of biomass ash content on biocomposite properties," *Compos. Part C Open Access* 9, article 100319. https://doi.org/10.1016/j.jcomc.2022.100319

Article submitted: April 20, 2026; Peer review completed: June 7, 2026; Revised version received and accepted: June 12, 2026; Published: July 8, 2026.
DOI: 10.15376/biores.21.3.7848-7870